Nano Today 61 (2025) 102604

Contents lists available at ScienceDirect

Nano Today

journal homepage: www.elsevier.com/locate/nanotoday

Engineered cytomembrane nanovesicles trigger *in situ* storm of engineered extracellular vesicles for cascade tumor penetration and immune microenvironment remodeling

Fei Sun [a,1], Shipeng Ning [b,1], Xiaoyuan Fan [c,1], Xia Wang [c,1], Ziqi Lin [a], Jian Zhao [a], Yutong Lu [a], Fengxiang Liu [a], Lili Du [a], Hao Zhang [a], Wenwen Shen [d], Jiaxin Lin [b], Zhonggui He [a,e], Kaiyuan Wang [a,*], Jin Sun [a,e,**]

[a] Department of Pharmaceutics, Wuya College of Innovation, Shenyang Pharmaceutical University, Shenyang, Liaoning 110016, China
[b] Department of Breast Surgery, The Second Affiliated Hospital of Guangxi Medical University, Nanning 530000, China
[c] School of Pharmacy, Shenyang Pharmaceutical University, Shenyang, Liaoning 110016, China
[d] Department of Pharmacy, The First Affiliated Hospital of Jinzhou Medical University, Jinzhou, China
[e] Joint International Research Laboratory of Intelligent Drug Delivery Systems, Ministry of Education, China

ARTICLE INFO

Keywords:
Tumor necrosis factor-α
Cytomembrane nanovesicles
Tumor penetration
Cancer immunotherapy
Membrane fusion

ABSTRACT

Immunotherapy for triple-negative breast cancer (TNBC) is hindered by its immunologically "cold" microenvironment, reducing treatment efficacy. Converting cold tumors into hot ones can significantly enhance the efficacy of immunotherapy. Nevertheless, the tumor extracellular matrix-associated physical barriers impede the infiltration of immunomodulating agents. Our previous research suggested that extracellular vesicles (EVs) secreted *in situ* by tumor cells could mediate the intercellular transport and deep infiltration of antitumor drugs. However, EVs' application faces obstacles such as inefficient delivery, lack of specificity, low production yields, and manufacturing inconsistencies. Based on this, we explored artificial cytomembrane nanovesicles (NVs) as the biomimetics of EVs. Herein, NVs are genetically engineered with membrane fusion-promoting protein VSVG to form VSVG-NVs (V-NVs). The calcium ionophore A23187 and plasmid encoding TNF-α with Lamp2b are loaded into V-NVs (V-NVs/T+A) using electroporation technology. The fusogenic VSVG component facilitates the integration of NVs with the target cancer cells and further incorporation into secreted EVs. The A23187 enhances EVs secretion by increasing intracellular calcium level. This synergistic approach ensures efficient intracellular delivery of TNF-α through EVs, facilitating deep tumor infiltration and remodeling of the immune microenvironment. As expected, the EV-hitchhiking strategy for cascade tumor deep penetration and immune microenvironment modulation demonstrates significant potential to enhance cancer immunotherapy.

Introduction

Breast cancer is the most common malignant tumor affecting women globally. Among these, triple-negative breast cancer (TNBC) is identified as the most aggressive subtype, commonly known as the most poisonous breast cancer [1–4]. In recent years, clinical trials have indicated that immunotherapy holds promise as a treatment modality for TNBC [5]. However, TNBC, characterized as a "cold tumor" [6–10], is defined by low immunogenicity and a suppressive tumor immune microenvironment, leading to the diminished effect of conventional immunotherapies [11–15]. A pressing challenge is how to facilitate the transition of "cold tumors" to "hot tumors" and reshape the immune microenvironment [16,17].

TNF-α, a cytokine predominantly produced by immune cells, plays a crucial role in the antitumor immune response, and directly acts on tumor cells, inducing cell death by activating apoptotic pathways within cancer cells [18–20]. Additionally, TNF-α has been reported to activate various immune cells, including macrophages, T cells, and B cells [21,

* Corresponding author.
** Corresponding author at: Department of Pharmaceutics, Wuya College of Innovation, Shenyang Pharmaceutical University, Shenyang, Liaoning 110016, China.
E-mail addresses: wangkaiyuan@hotmail.com (K. Wang), sunjin@syphu.edu.cn (J. Sun).
[1] These authors contributed equally to this work.

https://doi.org/10.1016/j.nantod.2024.102604
Received 4 September 2024; Received in revised form 9 December 2024; Accepted 15 December 2024

22]. However, the efficacy of TNF-α in tumor treatment is impeded by its limited penetration into dense tumor tissues [23]. This is primarily due to the tightly packed cellular architecture, thick extracellular matrix, and increased interstitial fluid pressure in the tumor microenvironment, which collectively create a barrier to TNF-α treatment [24–26]. Consequently, the suboptimal accumulation and intratumoral biodistribution of TNF-α result from the poor delivery efficiency, thereby reducing its therapeutic efficacy.

Extracellular vesicles (EVs), ranging from 30 to 150 nm, are composed of a lipid bilayer decorated with various transmembrane proteins [27–31]. EVs can transfer biologically active molecules between cells, thereby regulating gene expression and cellular function in recipient cells [32–34]. Moreover, through the intercellular transfer of functional membrane proteins layer by layer, we can modify tumor cells, alter their phenotype and enhance the immunogenicity, which further improves the tumor microenvironment for cancer immunotherapy [35, 36]. However, the EV-hitchhiking tumor penetration is typically limited by the unsatisfactory secretion efficiency of EVs [37,38].

Cytomembrane nanovesicles (NVs) are artificial membrane vesicles isolated from various cell types [39]. These vesicles can be engineered to deliver therapeutic agents [40,41]. Based on the above considerations, we ingeniously design membrane fusogenic NVs named as V-NVs/T+A. It is extracted from VSVG-expressing 4T1 cells, followed by the incorporation of A23187 and TNF-α-Lamp2b plasmid [42]. VSVG is a widely studied membrane fusion-promoting glycoprotein, which could mediate membrane fusion at acidic pH [43,44]. Modifying NVs with VSVG enables membrane fusion between NVs and target cells [43,45]. This strategy not only avoids the lysosomal degradation of TNF-α-Lamp2b plasmid, but also enables the translocation of A23187 and VSVG from NVs to cytomembrane [46]. A23187 is a calcium ionophore, which could increase intracellular calcium level, thereby stimulating the release of EVs and amplifying the efficiency of EV-hitchhiking tumor penetration [47–51]. Lamp2b is a commonly used exosome surface protein for targeting the exosome membrane. As a marker of EVs, Lamp2b ensures the targeted intracellular delivery of expressed TNF-α protein by sorting it into EVs, which in turn boosts the therapeutic efficacy of EVs [52,53]. By hitching a ride on tumor-secreted EVs, TNF-α are progressively delivered deeply into the solid tumor (Fig. 1). This ameliorates the tumor microenvironment and enhances the immune response against cancer. In summary, our findings provide a theoretical foundation for cascade tumor deep penetration and TNF-α cytokine therapy to enhance tumor immunotherapy.

Results and discussion

Preparation and characterization of V-NVs/T+A

Utilizing V-NVs as carriers, we loaded TNF-α-Lamp2b plasmids and A23187 through electroporation and incubation (Fig. 2A and Fig S1). Subsequently, different ratios were employed to determine optimal loading ratios for NVs, plasmids and A23187. The preferred ratio for subsequent experiments was established as NVs: plasmid = 2:1 and NVs: A23187 = 2:1. As shown in Fig. 2B–C, Fig. S2 and Table S1, particle size (~120 nm) was slightly larger than that of the blank NVs with negative zeta potential of around −30 mV. In the stability study conducted in PBS (pH 7.4) at 37°C for 12 h and storage at 4°C for 7 days, V-NVs/T+A exhibited minimal changes in particle size (Fig. 2D and Fig. S3). For long-term stable storage, V-NVs/T+A were lyophilized and subsequently reconstituted. As illustrated in Fig. S4, the particle size of V-NVs/T+A was remained stable after lyophilization indicating that no significant aggregation occurred after lyophilization. Furthermore, western blot results showed that the characteristic proteins on the

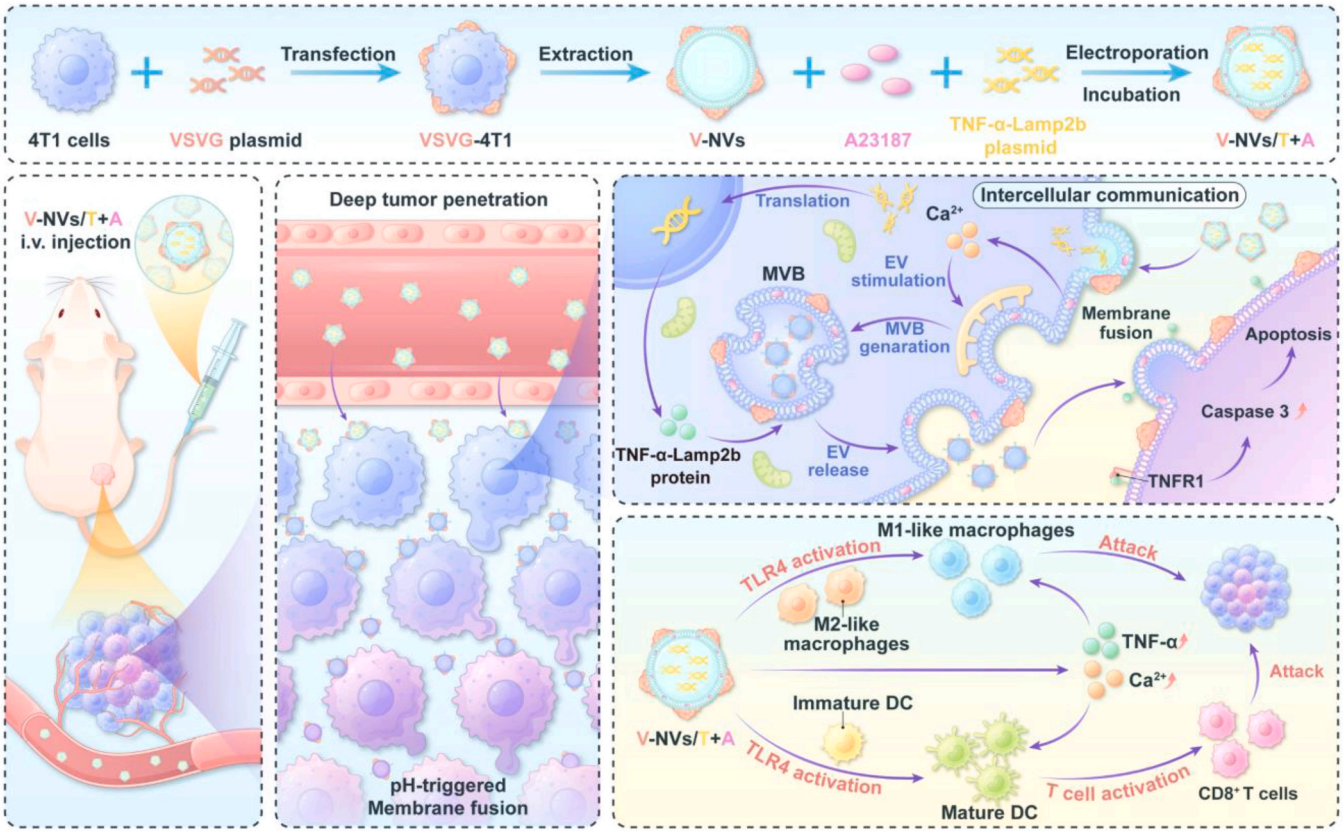

Fig. 1. The fabrication and biological functions of fusogenic cytomembrane nanovesicles. The innovative fusogenic nanovesicle platform, V-NVs/T+A, integrates a dual payload of A23187 and the TNF-α-Lamp2b plasmid, ensuring precise intracellular targeting while evading lysosomal clearance. This sophisticated design facilitates deep tumor penetration through an EV-hitchhiking mechanism, enhancing the microenvironment to stimulate a robust immune response against cancer.

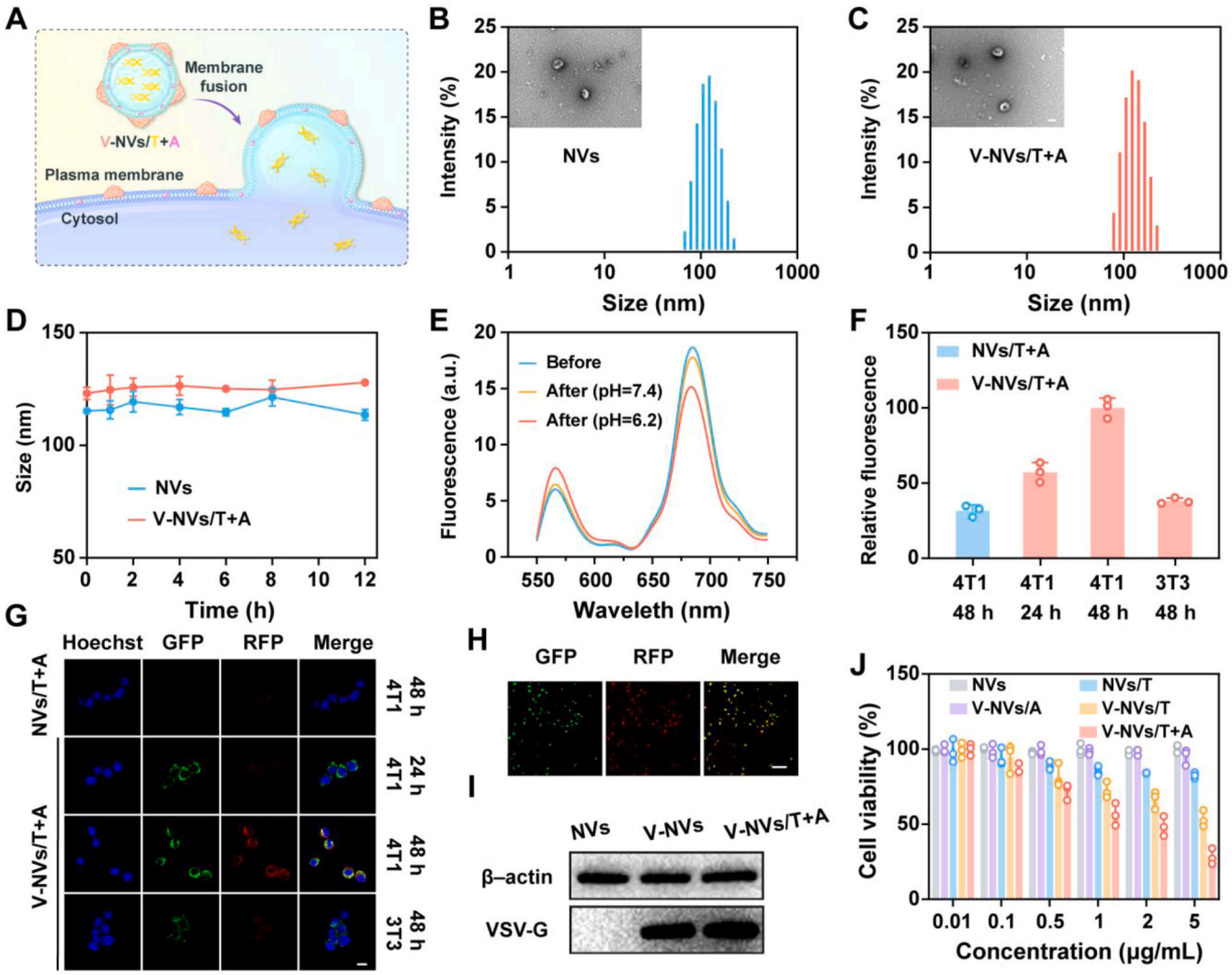

Fig. 2. Preparation and characterization of engineered NVs. (A) Schematic diagram of membrane fusion for V-NVs/T+A. Size distribution and electron microscopy images of NVs (B) and V-NVs/T+A (C). (Scale bar = 100 nm) (D) Stability of NVs and V-NVs/T+A. (E)The FRET effect curve between fluorescent liposomes and V-NVs at different pH levels. Cellular uptake of NVs/T+A and V-NVs/T+A in 4T1 and 3T3 cells, analyzed by flow cytometry (F) and CLSM (G). (Scale bar = 10 μm) (H) Colocalization of VSVG and TNF-α in cells after incubation with V-NVs/T+A. (Scale bar = 1 μm) (I) Expression of VSVG protein in cells after incubation with V-NVs/T+A. (J) Cytotoxicity to 4T1 cells.

surface of V-NVs/T+A remained unchanged (Fig. S5), indicating that the modification did not affect the inherent properties of the NVs. In addition, V-NVs/T+A has good loading efficiency for A23187 and plasmid (Table S2). These findings suggested that the V-NVs/T+A possessed favorable nanoparticulate properties and stability.

Functional validation of VSVG in V-NVs/T+A

To verify the successful transfection and function of VSVG on NVs membranes, we conducted the following experiments. First, western blot (WB) results demonstrated the expression of VSVG in V-NVs/T+A and flow cytometry indicating successful transfection with an efficiency of approximately 95 % (Fig. S6–S7). Then, we utilized fluorescence resonance energy transfer (FRET) to analysis the fusion activity of VSVG. It has been reported that under acidic conditions, VSVG can promote membrane fusion by interacting with LDLR and associated LDL family proteins on the cell surface. We prepared LDLR-functionalized liposomes loaded with fluorescent lipids, which were incubated with V-NVs for 30 min under acidic pH conditions resulting in the restoration of DiL fluorescence and a decrease in DiD fluorescence, indicating reduced FRET efficiency due to increased donor-acceptor distance and successful fusion of V-NVs with the fluorescently labeled liposomes, with a membrane fusion efficiency of 60 %. However, no significant fluorescence changes were observed under neutral pH condition. These findings demonstrated that the VSVG plasmid can be efficiently transfected into 4T1 cells and carried on NVs, but also enhance their membrane fusion capability (Fig. 2E).

Expression of the TNF-α-Lamp2b plasmid

Then the expression of plasmid in V-NVs/T+A was investigated. First, the mRNA levels of the TNF-α gene in 4T1 cells were evaluated through qRT-PCR. The results showed that TNF-α plasmids delivered through V-NVs/T+A were effectively transcribed within cells, leading to a sevenfold elevation in mRNA levels compared to cells treated with blank NVs (Fig. S8). Furthermore, quantitative analysis of TNF-α protein level in cell expression was conducted through enzyme-linked immunosorbent assay (ELISA). As depicted in the Fig. S9, the expressed TNF-α protein in V-NVs/T+A treated cells was approximately 580 pg/mL. These findings indicated the successful expression of TNF-α plasmid.

Investigation of cellular uptake mechanism

Given the crucial importance of cellular uptake of the V-NVs/T+A for anticancer efficacy, we further explored their uptake characteristics by flow cytometry and CLSM. As depicted in the Fig. 2F–G, the fluorescence intensity of V-NVs/T+A loaded with VSVG was significantly higher than that without VSVG and exhibited a time-dependent pattern. Notably, the V-NVs/T+A displayed reduced fluorescence intensity in 3T3 cells, attributed to the homotypic targeting property of the V-NVs/T+A derived from 4T1 cells, which exhibited restricted fusion ability with heterologous cells. These findings suggested that the V-NVs/T+A, facilitated by VSVG, can effectively fuse with homologous tumor cells, thereby exerting antitumor effects and reducing systemic toxicity. To further investigate the uptake mechanism of V-NVs, we used filipin, chlorpromazine, and wortmannin as inhibitors targeting caveolae-mediated endocytosis, clathrin-mediated endocytosis, and macropinocytosis, respectively. The results showed that the uptake of VSVG-modified NVs was not inhibited by any of these inhibitors, suggesting that the VSVG uptake mechanism may involve direct fusion of the VSVG-modified NVs with the 4T1 cell membrane (Fig. S10).

As depicted, co-localization of VSVG (green fluorescence) with TNF-α (red fluorescence) was observed in EVs treated with fluorescently labeled NVs, indicating the successful internalization of V-NVs/T+A (Fig. 2H). Western blot results (Fig. 2I) demonstrated the existence of VSVG protein in cells treated with NVs, confirming the successful uptake of NVs by the cells.

In vitro cytotoxicity

Following the successful expression of TNF-α plasmids in the V-NVs/T+A, we conducted *in vitro* assessments of their anti-tumor activity using the MTT assay (Fig. 2J). The V-NVs/T+A group exhibited noticeable anti-tumor effects, and the inclusion of VSVG significantly enhanced the efficacy, possibly due to its membrane fusion ability. Additionally, A23187 facilitated EVs secretion, promoting intercellular TNF-α transmission and enhancing anti-tumor activity.

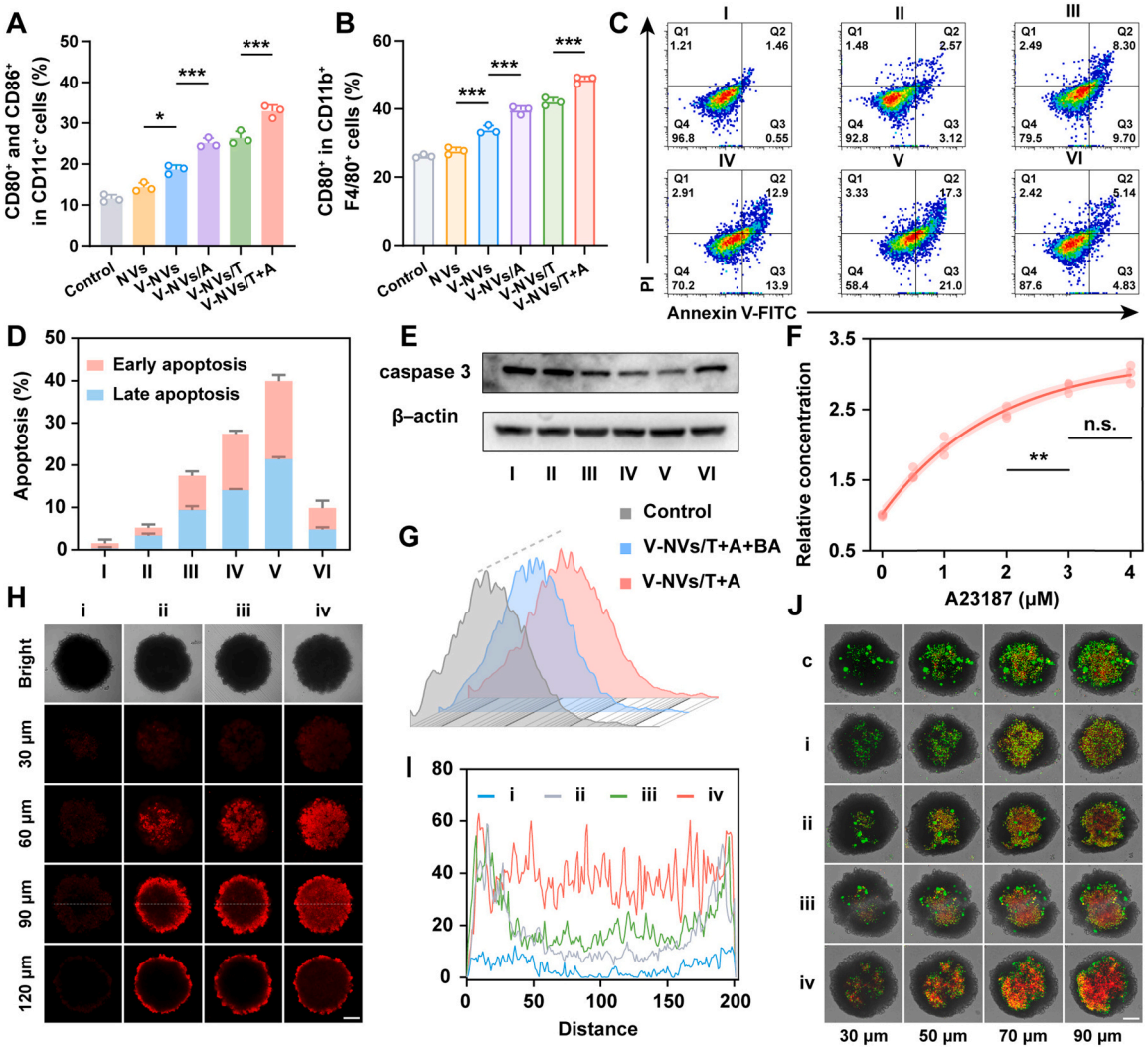

Fig. 3. *In vitro* evaluation of engineered NVs. Flow cytometry assessment of DC maturation ($CD45^+CD11c^+CD80^+CD86^+$) (A) and M1-like macrophages ($CD45^+CD11b^+F4/80^+CD80^+$) (B) triggered by different treatments in cancer cells (n = 3). (C) Flow cytometry analysis of apoptosis in 4T1 cells. (D) Quantitative analysis of cell apoptosis (n = 3). (E) Expression of apoptosis-related proteins in treated 4T1 cells. (F) A23187 promote EVs secretion in cells. (G) Fluo-2 probe used to mark Ca^{2+} in treated cells, with Ca^{2+} levels detected by flow cytometry. (H) Confocal microscopy examination of the penetration of V-NVs/T+A into tumor spheroids. (Scale bar = 100 μm) (I) Quantitative analysis of penetration. (J) CLSM of the cytotoxicity of V-NVs/T + A on tumor spheroids. Green: live cells. Red: dead cells. (Scale bar = 100 μm) I: Control, II: V-NVs/A, III: NVs/T, IV: V-NVs/T, V: V-NVs/T+A, VI: V-NVs/T+A+Z-VAD-FMK. c: Control, i: NVs/T, ii: V-NVs/T, iii: V-NVs/T+A+BA, iv: V-NVs/T+A. Data are represented as mean ± SD and statistical significance was carried out through one-way analysis of variance (ANOVA). * $p < 0.05$, ** $p < 0.01$, *** $p < 0.001$; n.s. indicates no significance.

Cellular immunity

Next, we investigated effects of the V-NVs/T+A on immune regulation. VSVG, recognized as a pathogen associated molecular pattern (PAMP) by innate immune cells, triggers innate immune responses that remodel the tumor microenvironment. When delivered to the tumor cell surface through V-NVs/T+A, it can induce allogeneic properties in the tumor cells, making them more recognizable to dendritic cells (DCs). Additionally, the influx of Ca^{2+} in tumors can regulate various immune cells, such as reprogramming tumor-associated macrophages, enhancing antigen presentation by DCs, and activating cytotoxic T lymphocytes. What's more, high expression of TNF-α at the tumor site can effectively stimulate DC maturation, while increased TNFR activation promotes the upregulation of the M1 phenotype and partially suppresses M2 gene expression.

To validate these effects, we conducted *in vitro* studies on the immunological responses of BMDCs and BMDMs co-cultured with tumor cell lines after treatment. The maturation of DCs was then quantified using double-positive cells for CD80 and CD86, revealing a marked increase in the number of mature DCs in V-NVs/T+A group, indicating enhanced antigen presentation capacity and stronger anti-tumor immunity. The V-NVs/T+A group showed a significant upregulation of CD80 compared to relevant controls, indicating that tumor cells incubated with the V-NVs/T+A can stimulate BMDMs to polarize towards the M1 phenotype (Fig. 3A–B and Fig. S11–S12). Thus, the V-NVs/T+A can systematically modulate immune cells from multiple aspects, including DC maturation and macrophage polarization, which are crucial for reshaping the tumor microenvironment in immunotherapy.

In vitro apoptosis assays

To further validate the anti-tumor effects of V-NVs/T+A, apoptosis assays were conducted with the addition of the TNF-α inhibitor Z-VAD-FMK. Flow cytometry results (Fig. 3C–D) showed a notable decrease in apoptosis following the addition of the TNF-α inhibitor, aligning with the observed cytotoxicity outcomes. These outcomes suggested that the V-NVs/T+A exhibit potent anti-tumor activity, with TNF-α being an important role. Moreover, the incorporation of VSVG and A23187 substantially enhanced the anti-tumor efficacy of TNF-α by promoting membrane fusion and intercellular communication. WB analysis demonstrated that stimulation with TNF-α specifically triggers the activation of caspases 3, leading to apoptosis and exerting an anti-tumor effect (Fig. 3E).

Intercellular communication

The intercellular transmission efficiency of V-NVs/T+A was verified through a transwell experiment. In Fig. S13, the continued presence of relevant fluorescence in the third layer of cells proved the effective intercellular transmission of TNF-α and VSVG by V-NVs/T+A. However, groups lacking VSVG and A23187 did not exhibit intercellular transfer, probably due to VSVG's cell membrane fusion promotion and A23187's enhancement of EVs secretion, which together facilitate the delivery of functional EVs between cells. After the addition of A23187 inhibitor, the diminished intercellular transmission ability further confirmed the essential role of intracellular Ca^{2+} level.

EVs extracted from V-NVs/T+A treated cells consistently showed intense TNF-α fluorescence, while the supernatant post-EVs separation lacked this fluorescence (Fig. S14), confirming TNF-α's selective incorporation into EVs. Fresh 4T1 cells treated with EVs showed significantly higher TNF-α levels compared to those treated with the supernatant (Fig. S15), confirming that TNF-α transfer mainly occurs through EVs.

Validation of the role A23187 in enhancing EVs secretion

A23187 significantly stimulates the release of EVs by increasing intracellular Ca^{2+} levels. BCA assay results suggested A23187 can stimulate a concentration-dependent increase in EVs production, with a plateau observed at 3 μM A23187 (Fig. 3F). The introduction of the calcium chelator BAPTA further supported the role of A23187 in EVs secretion (Fig. S16). We then utilized the Ca^{2+} sensitive probe Fura-2 AM to monitor changes in Ca^{2+} levels within 4T1 cells. Flow cytometry and confocal microscopy (Fig. 3G and Fig. S17) revealed a substantial increase in intracellular Ca^{2+} levels post-A23187 treatment. These results suggested that A23187 in the V-NVs/T+A can augment EVs release by elevating Ca^{2+} levels, thereby facilitating deeper intercellular communication.

Tumor spheroid penetration and cytotoxicity

We used 4T1 tumor spheroids as a model to investigate the deep intercellular delivery capability of NVs. The V-NVs/T+A showed the most effective penetration into tumor spheroids, as evidenced by significant TNF-α delivery to the spheroid core (Fig. 3H–I). This enhanced penetration was further validated by assessing the cytotoxicity of TNF-α in 4T1 tumor spheroids using live/dead cell staining. The results (Fig. 3J) confirmed that V-NVs/T+A induced significant cytotoxic effects, consistent with the cytotoxicity findings in tumor spheroids (Fig. S18).

In vivo pharmacokinetic and distribution

We further investigated the *in vivo* pharmacokinetics of V-NVs/T+A and its components A23187 and plasmids. As shown in Fig. S19, the detection of the fluorescent presence of A23187 and plasmids in the blood demonstrated their successful loading and release by V-NVs/T+A. The half-life of V-NVs/T+A cycle A23187 and plasmid was 2.19 h and 1.62 h, which was significantly longer than that of free component. These results indicated that V-NVs/T+A could significantly increase the circulating half-life of A23187 and plasmid.

In vivo distribution of NVs plays a critical role in determining their anti-tumor efficacy by affecting tumor targeting and retention. We evaluated the biodistribution of the V-NVs/T+A in 4T1 breast cancer-bearing mice. As shown in Fig. 4A and 4E, DiR Sol achieved maximum accumulation in the tumor site at 2 h post-administration, while the V-NVs/T+A reached their peak at 12 h due to the acidic response of VSVG, leading to greater tumor accumulation compared to NVs/T+A. Moreover, the NVs demonstrated higher tumor accumulation fluorescence at the tumor site within 24 h compared to DiR Sol. Subsequently, at the time of peak accumulation, major organs and tumors were isolated, and the results indicated that V-NVs/T+A had a higher tumor accumulation, indicating excellent tumor retention (Fig. 4B–D).

In vivo tumor penetration

In previous experiments, we validated that A23187 can increase the secretion of EVs from 4T1 tumor cells at the cellular level. To confirm the *in vivo* EVs secretion stimulating capability of V-NVs/T+A, we employed immunofluorescence staining targeting the EVs marker CD63 to assess EVs levels in tumor tissues. As shown in Fig. 4F, the results indicated that the group containing A23187 significantly promoted EVs secretion in the tumor microenvironment. This suggested that A23187 encapsulated in NVs can be effectively delivered to tumors, enhancing the secretion of EVs into the tumor microenvironment.

To investigate the infiltration of NVs within tumors, we administered DiR-labeled and unlabeled NVs intravenously into mice and collected tumor sections at 48 h post-injection. As shown in Fig. S20, substantial DiR fluorescence was detected in the deep tumor regions for the V-NVs/T+A group, consistent with our previous spheroid experiment findings. The consistent fluorescence observed in tumors demonstrated that TNF-α, facilitated by EVs, successfully penetrated deeply into the tumor tissue (Fig. 4G–H). In contrast, sections from the group without VSVG and

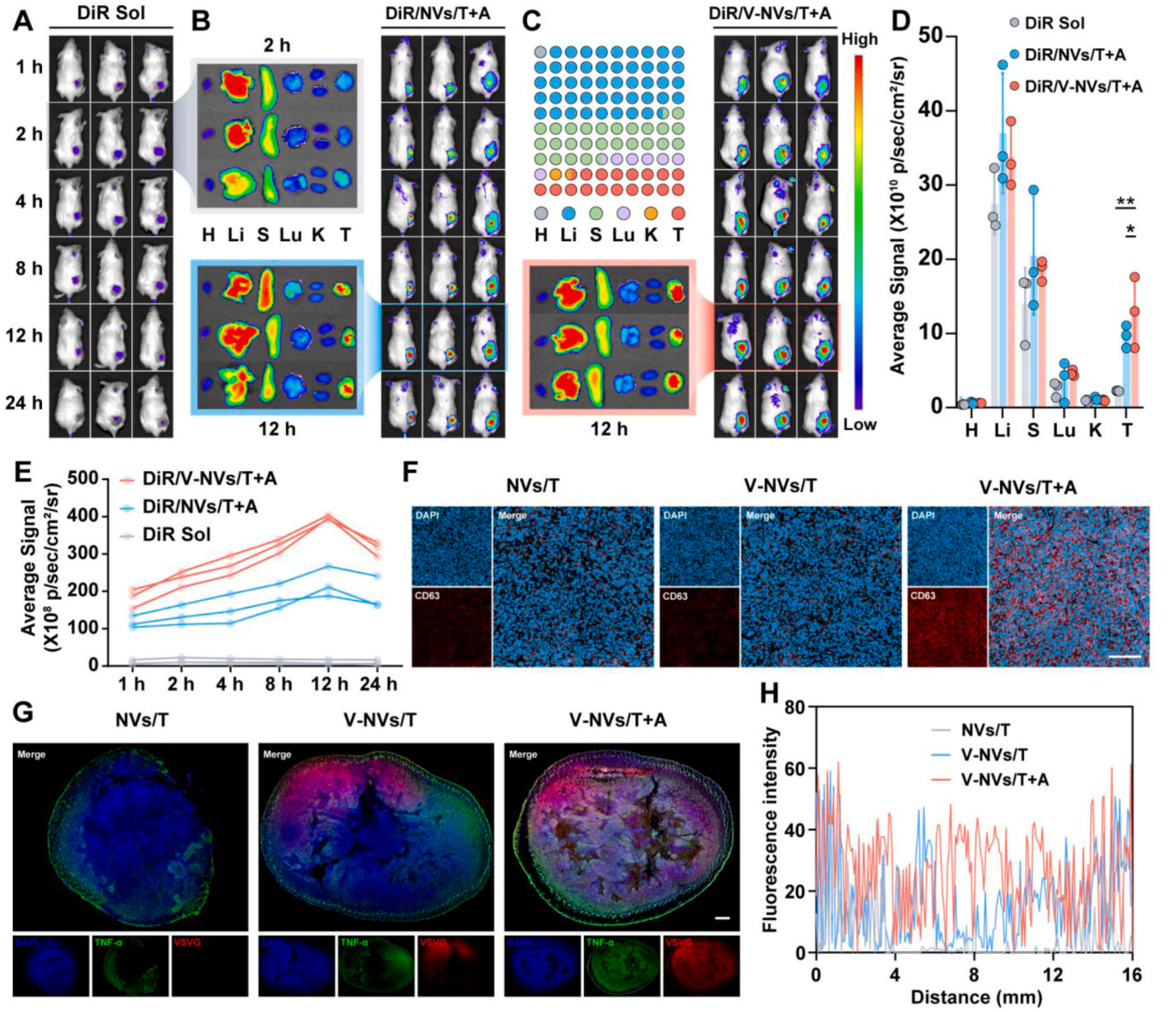

Fig. 4. *In vivo* distribution and penetration of engineered NVs. (A) *In vivo* images of 4T1 tumor-bearing mice after intravenous injection of V-NVs/T+A at predetermined time points (n = 3). (B) *Ex vivo* images of major organs and tumors in 4T1 tumor-bearing mice after intravenous injection of V-NVs/T+A (n = 3). (C) Distribution of V-NVs/T+A in different organs after injection at 12 h (n = 3). (D) Quantification of V-NVs/T+A in main organs after injection at 2 or 12 h. (E) Quantification of *in vivo* fluorescence intensity after injection of V-NVs/T+A (n = 3). (F) Confocal microscopy investigation of EVs secretion in 4T1 tumors. (Scale bar = 100 μm) (G) Confocal microscopy study and (H) semi-quantitative analysis on the penetration of V-NVs/T+A in 4T1 tumors. (Scale bar = 100 μm) (H: heart, Li: liver, S: spleen, Lu: lung, K: kidney, T: tumor).Data are represented as mean ± SD and statistical significance was carried out through one-way analysis of variance (ANOVA). *p < 0.05, **p < 0.01.

A23187 exhibited markedly reduced penetration. These results underscore the critical role of VSVG and A23187 in promoting the deep tumor infiltration of V-NVs/T+A.

In vivo anti-metastasis performance

Based on the preliminary validation, the V-NVs/T+A exhibit excellent *in vitro* performance and *in vivo* drug accumulation, including excellent stability and effective tumor penetration capabilities. These attributes hold promise for significantly enhancing anti-tumor immunotherapy *in vivo*, particularly in addressing the challenges of TNBC metastasis, such as lung invasion.

To evaluate its efficacy, we established a 4T1 tumor model in BALB/c mice by subcutaneously inoculating 4T1 cells and intravenously injecting 4T1-Luc cells to emulate malignant invasion and hematogenous spread (Fig. 5A). Using an *in vivo* luciferase imaging system, we monitored lung tumor progression. Compared to spontaneous metastasis, the systemic model, induced by intravenous injection of 4T1 cells, exhibits more aggressive metastatic behavior. *In vivo* imaging revealed reduced lung fluorescence intensity in the V-NVs/A and V-NVs/T groups, suggesting decreased metastatic growth, with V-NVs/T+A treatment further enhancing this effect, nearly abolishing fluorescence (Fig. 5B). *Ex vivo* bioluminescence imaging of the excised lung tissue corroborated these findings (Fig. 5D and Fig. S21). After fixation with Bouin's fluid, normal lung areas appeared yellow-brown, while metastatic nodules were bright yellow, aligning with bioluminescence data (Fig. 5C and 5E).

H&E staining after V-NVs/T+A treatment demonstrated a significant reduction in metastatic nodules in the liver and lung, with minimal detectable metastases (Fig. 5I–J). The V-NVs/T+A strategy not only

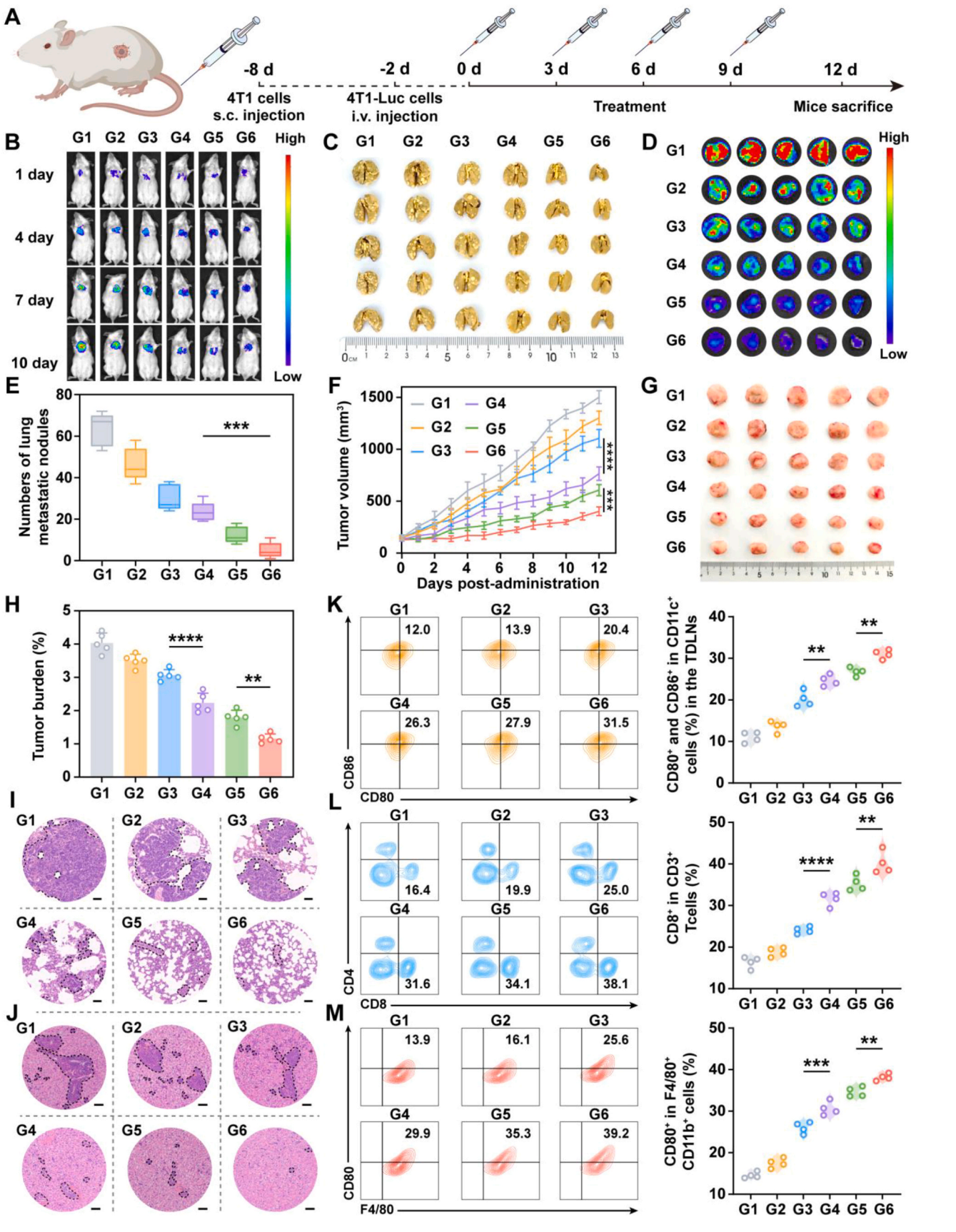

(caption on next page)

Fig. 5. *In vivo* anti-metastasis performance. (A) Schematic illustrating the administration strategy in a metastatic breast cancer model. (B) *In vivo* bioluminescence imaging of mice with 4T1-Luc metastatic tumors over time. (C) photograph of lung metastases for Bouin's fluid staining of lungs (n = 5). (D) *Ex vivo* IVIS bioluminescence imaging of excised lung tissues (n = 5). (E) Lung metastatic nodules quantification of (C) (n = 5). (F) Tumor growth curve after treatment. (n = 5). (G) Images of tumors. (n = 5). (H) Tumor-bearing rate (n = 5). H&E staining of the lung (I) and liver (J) slices after different treatments. (Scale bar = 50 μm) (K) Flow cytometry analysis of mature DCs ($CD45^+CD11c^+CD80^+CD86^+$) in mouse lymph nodes (n = 4). (L) Flow cytometry analysis of tumor-infiltrating $CD8^+$ T cells ($CD45^+CD3^+CD8^+$) (n = 4). (M) Flow cytometry analysis of M1-like macrophages ($CD45^+CD11b^+F4/80^+CD80^+$) (n = 4). G1: Saline, G2: NVs/T, G3: V-NVs, G4: V-NVs/A, G5: V-NVs/T, G6: V-NVs/T+A. Data are represented as mean ± SD and statistical significance was carried out through one-way analysis of variance (ANOVA). $^{**}p < 0.01$, $^{***}p < 0.001$, $^{****}p < 0.0001$.

inhibited metastasis but also reduced tumor volume compared to Saline, without affecting body weight or liver and kidney function parameters, indicating its safety (Fig. 5F–H and Fig. S22A–B). Tumor H&E staining (Fig. S22C) revealed increased necrotic areas, confirming the anti-tumor efficacy of V-NVs/T+A.

Further exploration of the anti-metastatic effect's association with immune modulation revealed increased CD86 and CD80 signals post-treatment, indicating elevated numbers of mature DCs. Additionally, there was a marked elevation in tumor-infiltrating $CD8^+$ T cells, indicative of enhanced cytotoxic immune responses, and a significant shift in macrophage polarization towards the M1-like phenotype, known for its pro-inflammatory and anti-tumor functions (Fig. 5K–M). These findings suggest that the V-NVs/T+A treatment not only suppresses tumor metastasis but also activates robust anti-tumor immunity.

In vivo antitumor activity

Orthotopic tumor models closely mimic the tumor microenvironment and metastatic behavior in mice, making them of paramount value for evaluating therapeutic efficacy. Consequently, we established an orthotopic BALB/c mouse model of 4T1 breast cancer to evaluate the *in vivo* anti-tumor efficacy of the V-NVs/T+A (Fig. 6A). As shown in Fig. 6B–D, the group without VSVG demonstrated minimal anti-tumor effects due to the inability to achieve membrane fusion and the group treated with one agent showed weak immune response. Notably, the V-NVs/T+A showed great potential in immune activation, exhibiting the optimal anti-tumor effects with a tumor inhibition rate exceeding 70 % (Fig. 6E). H&E staining and TUNEL assay results further revealed the potent destructive effect of the V-NVs/T+A (Fig. 6I). Furthermore, we evaluated the safety of the V-NVs/T+A *in vivo*. As illustrated, no obvious abnormalities were observed in the H&E-stained sections of major organs (heart, liver, spleen, lung, kidney) or in the blood parameters of the liver and kidney after treatment (Fig. 6H and Fig. S23) and there were no significant changes in mouse weight during the treatment period (Fig. 6G). Furthermore, we have measured the levels of secretion of proinflammatory cytokines. V-NVs/T+A treatment led to high expression of proinflammatory cytokines in serum including TNF-α, IFN-γ, and IL-6 (Fig. 6F).

The exploration of anti-tumor mechanisms

In vivo experiments have demonstrated the potent anti-tumor effects of V-NVs/T+A. Consequently, we further investigated their anti-tumor mechanisms by examining the changes in the tumor immune microenvironment post-treatment (Fig. S24–S26 and Table S3). Encouragingly, compared to other groups, the increased CD86 signal after V-NVs/T+A treatment indicated a significant rise in the number of mature dendritic cells (DCs) (Fig. 7B). These mature DCs ($CD45^+CD11c^+CD80^+CD86^+$) can present antigens to T lymphocytes, thereby initiating tumor-specific adaptive immunity. As anticipated, the number of tumor-infiltrating $CD8^+$ T cells ($CD45^+CD3^+CD8^+$) increased by 2.04-fold following V-NVs/T+A treatment (Fig. 7A and 7C), while immunosuppressive regulatory T cells (Tregs, $CD45^+$ $CD3^+CD4^+Foxp3^+$) decreased by 0.54-fold compared to the control group (Fig. 7D), indicating a robust T cell-mediated immune response triggered by V-NVs/T+A. We observed similar synergistic effects in macrophages. Compared to the control group, M2-like tumor-associated macrophages ($CD45^+CD11b^+F4/80^+CD206^+$) were decreased, while M1-like tumor-associated macrophages ($CD45^+CD11b^+F4/80^+CD80^+$) were significantly elevated, further confirming the activation of anti-tumor immunity (Fig. 7E–F). We performed TNF-α immunofluorescence staining on tumor sections to evaluate TNF-α distribution within the tumor microenvironment. The V-NVs/T+A treatment group showed the strongest TNF-α signal, indicating effective accumulation and penetration of TNF-α into the tumor tissue. This elevated TNF-α presence in the V-NVs/T+A group supports its role in enhancing local immune activation, contributing to a robust anti-tumor response (Fig. S27). TNF-α^+ and IFN-γ^+ $CD8^+$ T cells are crucial for anti-tumor immunity, as they directly kill tumor cells and activate surrounding immune responses. We further assessed the levels of TNF-α^+ and IFN-γ^+ in $CD8^+$ T cells and observed a significant increase, aligning with the enhanced anti-tumor response facilitated by V-NVs/T+A treatment. (Fig. 7G–H and Fig. S28) This result demonstrates the effective delivery and penetration of TNF-α within the tumor microenvironment, further amplifying the anti-tumor efficacy of V-NVs/T+A.

Conclusions

In summary, we have developed a novel strategy to enhance immune response by harnessing NVs to facilitate the deep penetration of TNF-α. This study elucidated the comprehensive engineering process of NVs. Furthermore, a series of evaluations had demonstrated the significant potential of V-NVs/T+A in achieving deep tumor penetration and enhancing TNF-α immunotherapy. This represents a methodological advancement that addresses the challenges of poor immunotherapy efficacy due to inhibitory tumor microenvironments and low immunogenicity. Our research presents a new therapeutic modality to overcome the barriers to immunotherapy in cold tumor.

Experimental section/methods

Materials

$DSPE\text{-}mPEG_{2k}$ was obtained from AVT (Shanghai) Pharmaceutical Tech Co., Ltd. The plasmid encoding VSVG and TNF-α-Lamp2b were constructed by Sangon Biotech (Shanghai) Co., Ltd. DiR was purchased from Shandong Sparkjade Biotechnology Co., Ltd. BCA Protein Content Assay kit (AKPRO17) was purchased from Beijing Boxbio Science & Technology Co., Ltd. BAPTA-AM was purchased from Macklin Biochemical Co., Ltd (Shanghai, China). 18:1 DGS-NTA (Ni) was obtained from Aladdin (Shanghai, China). Fura-2 AM, Z-VAD-FMK and the reagents applied in Western blot assay were obtained from Dalian Meilun Biotechnology Co., Ltd (China). The calcein-AM/PI live/dead cell staining kit and Annexin V-FITC Apoptosis Detection Kit were acquired from Beijing Solarbio Science & Technology Co., Ltd. TNF-α (JL10484) ELISA kit was purchased from Jianglai biology, Shanghai. Cell culture medium and glass-bottom dishes were obtained from NEST Biotechnology Co., Ltd. (Wuxi, China).

Preparation of engineered NVs

4T1 cells were initially plated in dishes and incubated for 12 h. The transfection reagent and VSVG plasmid were separately diluted in Opti-MEM medium and mixed for 15 min. Then, the cell culture medium was

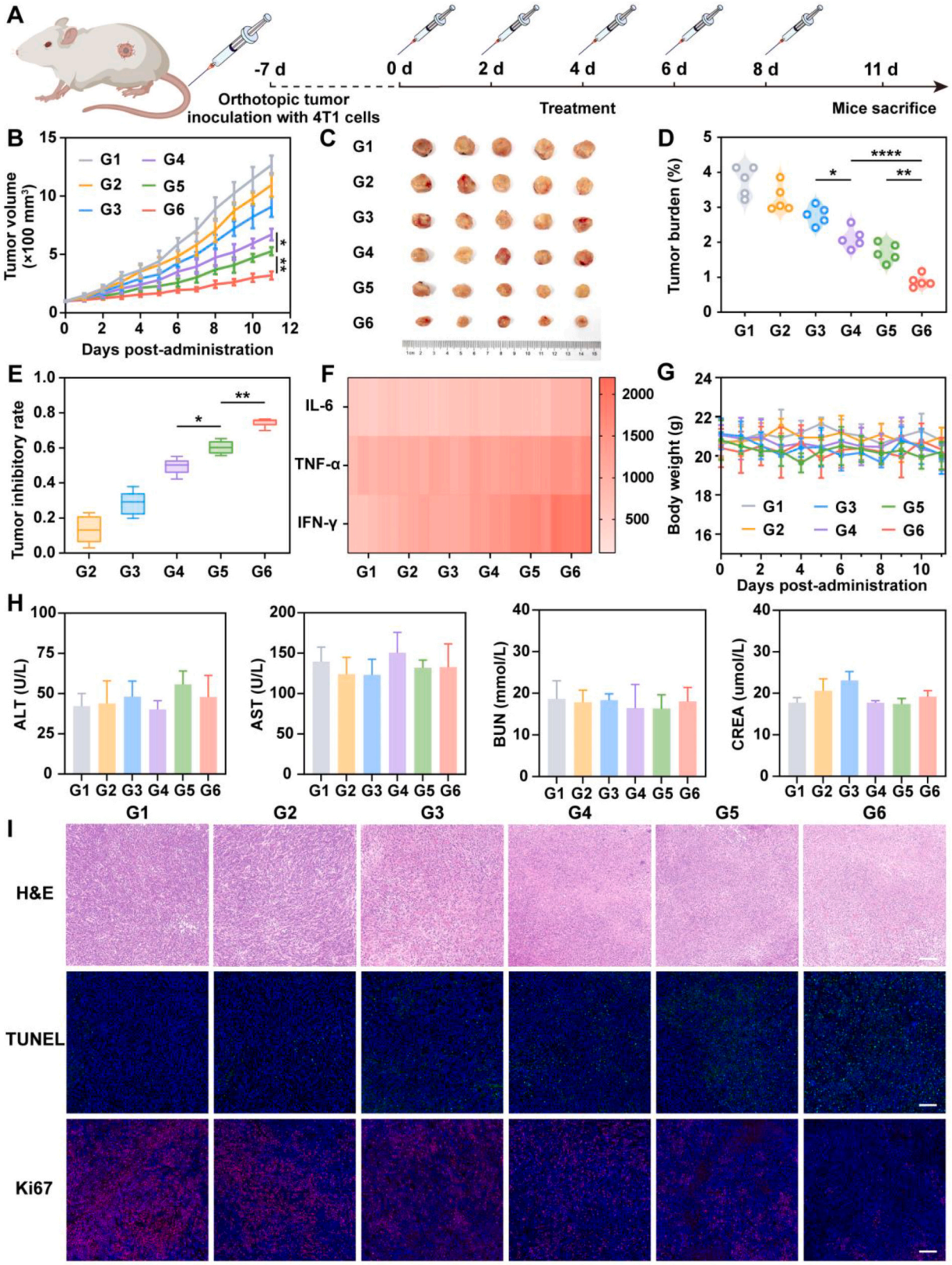

Fig. 6. *In vivo* antitumor evaluation. (A) Schematic representation of mouse administration. (B) Tumor growth curve after treatment (n = 5). (C) Images of tumors (n = 5). (D) Tumor bearing rate (n = 5). (E) Tumor inhibition rate (n = 5). (F) Secretion of pro-inflammatory cytokines (TNF-α, IFN-γ, IL-6) in tumor supernatant of 4T1 tumor model (n = 4). (G) Changes in mouse body weight during treatment (n = 5). (H) Changes in liver and kidney function indicators in tumor-bearing mice after the last treatment (n = 4). (I) H&E, TUNEL, Ki67 staining images of tumors after treatment. (Scale bar = 100 μm). G1: Saline, G2: NVs/T, G3: V-NVs, G4: V-NVs/A, G5: V-NVs/T, G6: V-NVs/T+A. Data are represented as mean ± SD and statistical significance was carried out through one-way analysis of variance (ANOVA). *$p < 0.05$, **$p < 0.01$, ****$p < 0.0001$.

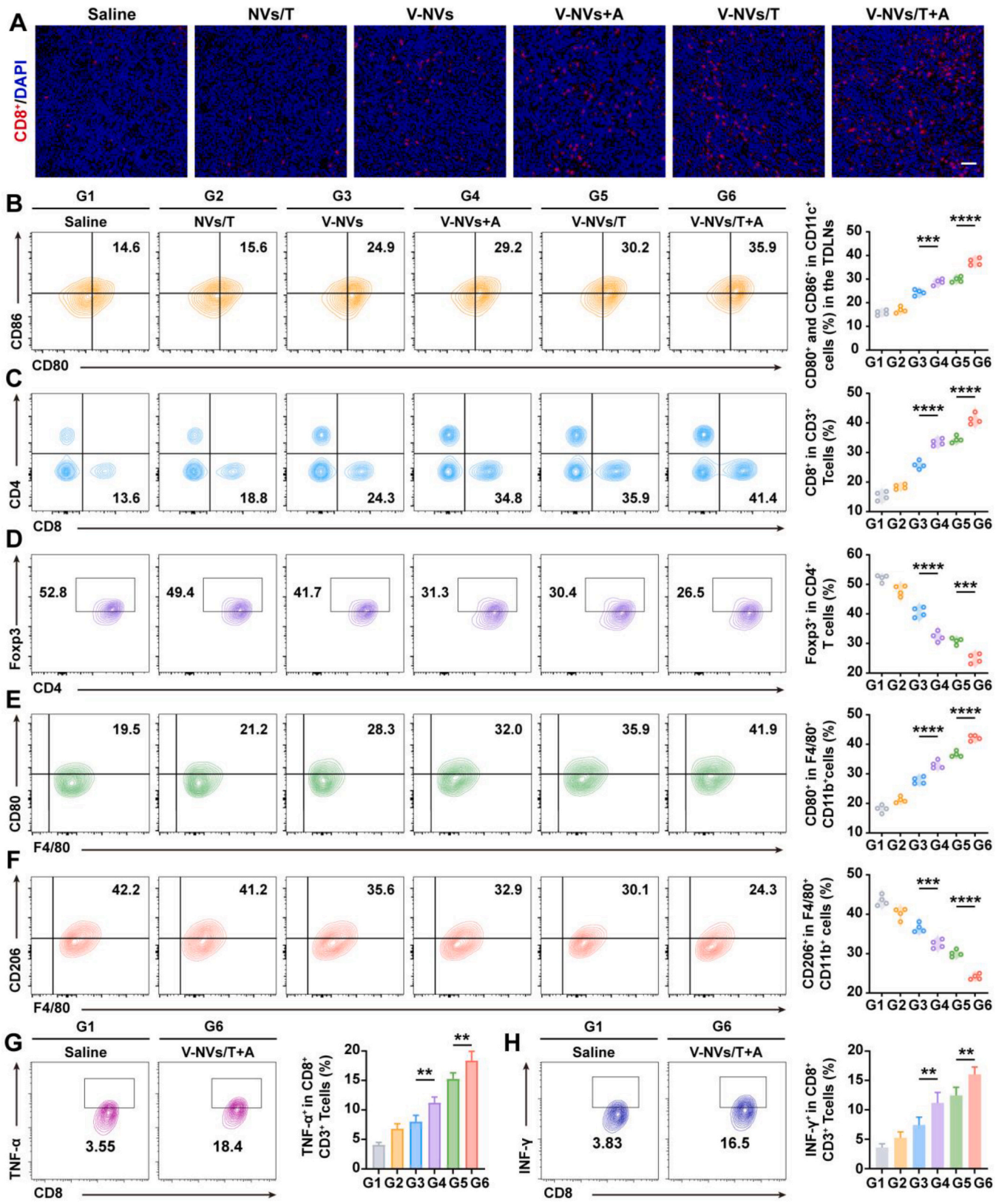

Fig. 7. (A)Immunofluorescence images of $CD8^+$ T cells in tumor slices. (Scale bar =50 μm) (B) Flow cytometry analysis of mature DCs ($CD45^+CD11c^+CD80^+CD86^+$) in mouse lymph nodes (n = 4). (C) Flow cytometry analysis of tumor-infiltrating $CD8^+$ T cells ($CD45^+CD3^+CD8^+$) (n = 4). (D) Flow cytometry analysis of tumor-infiltrating regulatory T cells (Tregs, $CD45^+CD3^+CD4^+Foxp3^+$) (n = 4). Flow cytometry analysis of tumor-infiltrating M2-like macrophages ($CD45^+CD11b^+F4/80^+CD206^+$) (E) and M1-like macrophages ($CD45^+CD11b^+F4/80^+CD80^+$) (F) (n = 4). (G) Flow cytometry analysis of TNF-α^+ $CD8^+$ T cells ($CD45^+CD3^+CD8^+TNF\text{-}\alpha^+$) in tumor tissues. (H) Flow cytometry analysis of IFN-γ^+ $CD8^+$ T cells ($CD45^+CD3^+CD8^+IFN\text{-}\gamma^+$) in tumor tissues. G1: Saline, G2: NVs/T, G3: V-NVs, G4: V-NVs/A, G5: V-NVs/T, G6: V-NVs/T+A. Data are represented as mean ± SD and statistical significance was carried out through one-way analysis of variance (ANOVA). $^{**}p < 0.01$, $^{***}p < 0.001$, $^{****}p < 0.0001$.

replaced with Opti-MEM medium, and the mixed solution was added to the cells. After 48 h, the cells were resuspended in PBS and sonicated in the sterile EP tube (22 W, 4°C) for 60 s using the ultrasonic crusher Cellular debris, then the NVs were removed by serial centrifugation (10 min at 2000 r.p.m., 10 min at 5000 r.p.m., and 60 min at 15000 r.p.m.). After the first two centrifugations, the supernatant was collected, and the pellets were discarded. In the final centrifugation, the pellets were resuspended in PBS. The supernatant was filtered through a 0.22 μm filter to collect V-NVs. The protein concentration of the V-NVs was quantified by BCA protein assay kit. The V-NVs and TNF-α-Lamp2b plasmid were mixed in a 2:1 ratio of V-NVs protein to plasmid in a chilled 0.4 cm cuvette. Electroporation was performed using a BioRad device (USA) with settings of 400 V voltage, 25 μF capacitance, 50 Ω resistance, and a pulse duration of 10–15 ms. After electroporation, the mixture was incubated at 37°C for 30 min to allow the vesicle membrane to recover, resulting in V-NVs/T. Finally, A23187 was added to the V-NVs/T mixture at a 2:1 ratio of V-NVs protein to A23187 and incubated for 30 min at 37°C to obtain V-NVs/T+A.

Characterization of engineered NVs

The particle sizes and zeta potentials of NVs and V-NVs/T+A were analyzed by dynamic light scattering (DLS) using the ZetaSizer (Nano ZS, Malvern Co., UK). The structures of prepared NVs and V-NVs/T+A were detected by transmission electron microscopy (TEM, Hitachi, HT7700, Japan) with uranyl acetate solution. The NVs and V-NVs/T+A were incubated in PBS (pH 7.4) at 37°C or 4°C in a shaker. The shaker speed was set to 100 rpm to ensure proper agitation during incubation. The stabilities of NVs and V-NVs/T+A were evaluated by measuring the changes of particle sizes at different times by the ZetaSizer. To assess the lyophilization stability of the NVs and V-NVs/T+A, 1 mg/mL samples were subjected to the lyophilization process. The samples were frozen at −80°C before lyophilization, and trehalose (50 mM) was added as a cryoprotectant to safeguard the structure during the freezing process. The stability was evaluated by examining the lyophilized appearance and particle size post-reconstitution.

Cell line and cell culture

4T1 and 3T3 cell lines were procured from the Cell Bank of Type Culture Collection of Chinese Academy of Sciences (Shanghai, China). The 4T1 cells were cultured in RPMI 1640 medium supplemented with 10 % FBS and 1 % penicillin-streptomycin, while the 3T3 cells were cultured in DMEM/F-12 medium containing the same supplements. All cells were maintained under an atmosphere of 5 % CO_2 at 37°C. It was confirmed that there was no mycoplasma contamination in any of the cell lines used in this research.

Western blotting assay

Proteins obtained from V-NVs/T+A or cells were isolated and quantified using a BCA kit. Following this, equal protein amounts (40 μg) from each sample were subjected to separation via SDS-PAGE. The proteins then transferred to PVDF membranes were blocked with 5 % skim milk. This was followed by an overnight incubation at 4°C with primary antibodies, including CD9 (ab236630, Abcam, 1:1000 dilution), CD81 (ab79559, Abcam, 1:1000 dilution), Na/K ATPase (ab254025, Abcam, 1:1000 dilution), VSVG (ab50549, Abcam, 1:1000 dilution), β-actin (ab6276, Abcam, 1:5000 dilution) and caspase-3 (ab32351, Abcam, 1:1000 dilution). Primary antibody and secondary antibody incubation were performed in TBST with 5 % skim milk to reduce non-specific binding. Then, the PVDF films were incubated with HRP Goat Anti-Rabbit IgG H&L (ab6721, Abcam, 1:5000 dilution) for another 2 h. Chemiluminescence detection was carried out for protein band visualization with ECL luminescence reagent.

Membrane fusion characteristics of V-NVs/T+A

To analyze the efficiency of membrane fusion via FRET effect, we prepared FRET liposomes using DiL and DiD as the fluorescent donor and acceptor, respectively, at a molar ratio of 1:7. In brief, the lipid mixture was initially dried under vacuum and then rehydrated with PBS. Following five freeze-thaw cycles, large unilamellar vesicles were prepared by extrusion through a 200 nm polycarbonate filter. These liposomes were labeled with DiD and DiL, then immobilized on a PEG-coated surface via streptavidin-biotin lipid conjugation. The LDLR was then tethered to the liposomes using the Ni-NTA system. Subsequently, V-NVs were introduced and incubated under pH 6.2 and pH 7.4 at 37°C. Measured the fluorescence spectra in the range of 550 nm ~ 750 nm to assess fusion.

Expression of the TNF-α-Lamp2b plasmid

The content of TNF-α was determined using an ELISA kit, following the manufacturer's protocol. For mRNA analysis, 4T1 cells subjected to various treatments were incubated for 48 h, rinsed with PBS, and total RNA was extracted using the HiPure Universal RNA Mini Kit (Guangzhou Magen Biotechnology Co., Ltd.) with 500 μL lysis buffer per sample. RNA concentration was measured using a NanoDrop 2000 (Thermo Scientific), and 1 μg of total RNA was reverse-transcribed into cDNA using the HiScript II Reverse Transcriptase kit (Vazyme Biotech Co., Ltd.). Quantitative detection of mRNA expression was performed using StarLighter SYBR Green qPCR mix (Beijing Foreverstar Biotech) with the following conditions: 95°C for 30 s for Taq activation, followed by 30 cycles of 95°C for 10 s and 60°C for 30 s. TNF-α primers were forward: 5′-caggcggtgcctatgtctc-3′ and reverse: 5′-cgatcaccccgaagttcagtag-3′. Relative gene expression levels were calculated using the $2^{-\Delta\Delta Ct}$ method with GAPDH for normalization, and all experiments were performed in triplicate for reliability.

Cellular uptake

4T1 and 3T3 cells were seeded in confocal dishes (1050001, SAINING Biotechnology) at a density of 5×10^4 cells and cultured for 12 h. Subsequently, to assess cellular uptake efficiency, we fused the VSVG protein with green fluorescent protein (GFP) and marked TNF-α with red fluorescent protein (RFP). 4T1 cells and 3T3 cells were treated separately with V-NVs/T+A and incubated for 24 h or 48 h. Following removal of the culture medium, cells were washed, stained with Hoechst, and observed under a confocal laser scanning microscope (CLSM, C2, Nikon, Japan). For quantitative analysis, 4T1 and 3T3 cells (5×10^5 cells per well) were seeded in 12-well plates and pretreated with the same concentrations of filipin (7.5 μM), chlorpromazine (30 μM), and wortmannin (5 μM) before adding NVs. After incubation and treatment, cells were washed, collected, and analyzed by flow cytometry (LongCyte, Beijing Challen Biotechnology Co., Ltd.) to assess cellular uptake efficiency. Western Blot (WB) was conducted to confirm the expression of VSVG protein in cells treated with NVs. Afterwards, EVs were extracted from 4T1 cells treated with engineered NVs and observed using CLSM.

Cellular immune activation

Bone marrow cells were harvested from the tibias and femurs of 6–10-week-old BALB/c mice. The bones were dissected, cleaned of surrounding muscle tissue, sterilized with 70 % ethanol for 2–5 min, and washed twice with sterile PBS. Bone marrow was flushed out with cold PBS using a syringe, filtered through a 70 μm mesh, and centrifuged at 1200 rpm for 5 min. These cells were cultured in RPMI 1640 medium supplemented with 1 % penicillin-streptomycin and 10 % bovine serum. To facilitate differentiation into bone marrow-derived dendritic cells (BMDCs) and bone marrow-derived macrophages (BMDMs), the cultures

were treated with recombinant mouse granulocyte-macrophage colony-stimulating factor (GM-CSF) at 20 ng/mL and recombinant mouse interleukin-4 (IL-4) at 10 ng/mL for BMDCs, or granulocyte-macrophage colony-stimulating factor (M-CSF) at 20 ng/mL for BMDMs, respectively. The medium was refreshed every other day, and the cells were cultured for a total of seven days to allow differentiation into BMDCs and BMDMs. The immature BMDCs and BMDMs were then co-cultured with 4T1 tumor cells that had been treated with V-NVs/T+A for 48 h. Subsequently, flow cytometry analysis was performed using antibodies against CD45, CD11c, CD80 and CD86 for the BMDCs, and CD45, CD11b, F4/80 and CD80 for the BMDMs.

Cytotoxicity assays

The anti-proliferative activity of V-NVs/T+A was assessed using MTT assay. 4T1 cells were seeded at a density of 1×10^3 cells per well in 96-well plates and incubated for 12 h. After removing the culture medium, cells were treated with V-NVs/T+A and incubated for 48 h. MTT solution was then added and incubated for an additional 4 h. The MTT solution was replaced with dimethyl sulfoxide (DMSO), and cell viability was measured at 490 nm using a microplate reader (Thermo Scientific, USA).

Cellular apoptosis

4T1 cells were seeded at a density of 5×10^5 cells per well in 12-well culture plates (PakGent Bioscience (Suzhou) Co., Ltd.) and incubated for 12 h. Subsequently, the cells were treated with V-NVs/T+A and Z-VAD-FMK (20 μmol/L), an inhibitor of TNF-α-induced cytotoxicity. After 48 h, the previously used cell culture medium was collected into centrifuge tubes. The Cells were then digested, and digestion was terminated by adding the previously collected medium. After centrifuging and resuspending the cells, the supernatant was collected after a second centrifugation. Annexin V-FITC apoptosis detection kit was used to stain the cells, followed by immediate analysis through flow cytometry. Western blot analysis was performed to assess the expression levels of caspase-3 activated by TNF-α in the cells.

Mechanism verification of A23187

4T1 cells were seeded at a density of 1×10^6 cells per well in 6-well plates and incubated for 12 h. The cells were treated with A23187 Sol, V-NVs/T+A, or NVs containing the calcium ion chelator BAPTA to verify the effect of A23187 on promoting EVs release. To further investigate the mechanism by which A23187 promotes EVs release, intracellular Ca^{2+} levels were monitored using the Ca^{2+}-sensitive probe Fura-2 AM. Changes in Ca^{2+} levels were quantified by flow cytometry and validated using confocal laser scanning microscopy (CLSM).

Validation of intercellular transfer mechanism

The intercellular transmission capability was evaluated using transwell experiments. 4T1 cells were seeded in transwell plates (Kirgen Bioscience (Shanghai) Co., Ltd.) or 12-well culture plates. After 12 h incubation, fluorescently labeled V-NVs/T+A were applied to the cells in the upper chamber. Following 2 h incubation, the V-NVs/T+A were washed away by PBS. After 48 h, the cells in the lower chamber of the culture plate were digested, reseeded into new upper chambers, and new 4T1 cells were introduced into the lower chamber of the transwell. Finally, the transfer of EVs between cells was observed using CLSM. In parallel, to investigate the transmission mechanism, EVs and supernatant were extracted from 4T1 cells treated with V-NVs/T+A in 12-well plates, and their fluorescence was quantified using a microplate reader. The extracted EVs and supernatant were then incubated with fresh cells, and flow cytometry was performed to further assess the transmission efficiency.

Tumor spheroid penetration efficiency

A tumor spheroid model was established to investigate the drug permeability and tumor inhibitory effects. Briefly, 1×10^4 4T1 cells were seeded in a medium containing consisting of 0.24 % methylcellulose mixed with 1640 medium at a 1:1 ratio and dispensed onto the lids of round-bottom 96-well plates. Following 24 h incubation in a cell culture incubator, 200 μL of complete culture medium was added to each well. The cell spheroids were then centrifuged at 2800 rpm for 3 min, facilitating their transfer from the lids to the wells. Subsequent culturing involved medium replacement every 48 h. On the fourth day, the supernatant was aspirated, and the medium was substituted with either fluorescently labeled or non-fluorescently labeled V-NVs/T+A. The spheroids were incubated for an additional 48 h. The medium was removed post-incubation, and the spheroids were rinsed with PBS. The penetration of fluorescence within the tumor spheroids was assessed using CLSM. The treated spheroids were stained with Calcein-AM (4.5 mM) and PI (2 mM) for 30 min, allowing for the visualization of live and dead cells within the spheroids using the same imaging modality.

The tumor spheroids were collected by centrifugation, and dissociated into single cells using fivefold diluted trypsin, followed by another round of centrifugation. 20 μL of MTT solution was added to each well, and the cells were incubated at 37°C for 4 h. Post incubation, the supernatant was removed and 200 μL of DMSO was added. Then, measured the absorbance at 490 nm using a microplate reader to calculate cell viability.

Animal

BALB/c mice (female) were supplied by the Animal Center of Shenyang Pharmaceutical University (Shenyang, Liaoning, China). The use of animals is approved by the Animal Ethics Committee of Shenyang Pharmaceutical University.

In vivo pharmacokinetic and distribution

The BALB/c mice were intravenously injected with A23187 Sol, Cy5-Plasmid Sol, and V-NVs/T+A, with each mouse receiving 100 μg of V-NVs/T+A. Blood samples were collected at various time points (0.033, 0.083, 0.25, 0.5, 1, 2, 4, 8, and 12 h) and serum was harvested. Fluorescence of A23187 was measured using a plate reader at λ_{ex}= 378 nm and λ_{em}= 430 nm and fluorescence of Cy5-Plasmid was measured at λ_{ex}= 650 nm and λ_{em}= 670 nm. The concentrations of A23187 and plasmid were obtained according to the standard curves.

4T1 cells (1×10^6 cells) were injected into the female BALB/c mice. In order to achieve real-time evaluation on the biodistribution of V-NVs/T+A by fluorescence imaging, DiR was utilized to label the NVs (DiR-NVs/T+A and DiR-V-NVs/T+A) at a dosage of 1 mg/kg DiR equivalent. When the subcutaneous 4T1 tumor volume reached approximately 200 mm^3, we administered DiR Sol, DiR-NVs/T+A and DiR-V-NVs/T+A via intravenous injection (n = 3). At predetermined time points (2, 4, 8, 12, and 24 h), we anesthetized mice and conducted images using IVIS imaging system. Mice were euthanized at 4, 12, and 12 h post-administration, major organs and tumors were collected for analysis using the IVIS imaging system.

In vivo penetration experiments

BALB/c mice bearing 4T1 tumors were intravenously injected with DiR-labeled NVs (NVs/T, V-NVs/T, and V-NVs/T+A) or their unlabeled counterparts at a dosage of 100 μg NVs per mouse. After 48 h, tumors were harvested, fixed in 4 % paraformaldehyde, embedded in paraffin, and sectioned into 5 μm-thick slices. Tumor slices from the DiR-labeled groups were subjected to CD31 immunofluorescence staining to visualize tumor vasculature and assess drug penetration under a confocal

laser scanning microscope (CLSM). Fluorescence quantification was performed using ImageJ software to compare the penetration efficiency of V-NVs/T+A. For the unlabeled NVs groups (NVs, V-NVs/T, and V-NVs/T+A), tumor slices were stained with CD63, anti-TNF-α and anti-VSVG antibodies. Appropriate fluorescently labeled secondary antibodies were applied. The samples were imaged using CLSM, and the fluorescence signals of TNF-α and VSVG were quantified using ImageJ to evaluate delivery efficiency and distribution patterns within the tumor.

In vivo anti-metastasis performance

4T1 cells (1×10^6 cells) were injected into the female BALB/c mice. Six days later, to simulate a more malignant invasion and hematogenous metastasis, each mouse was intravenously injected with a 4T1-Luc cell suspension of 100 μL. After two days of inoculation, the mice are divided into six groups and treated with Saline, NVs/T, V-NVs, V-NVs/A, V-NVs/T, V-NVs/T+A. Treatments were administered every three days for four cycles, with a dosage of 100 μg NVs per cycle. One day after each administration, the mice were intraperitoneally injected with D-Luciferin solution (15 mg/mL). 10 min later, bioluminescence was immediately detected and analyzed using an *in vivo* bioluminescent imaging to assess cancer metastasis.

After the final treatment, mice were euthanized, and their lungs were promptly harvested to assess cancer metastasis. Lung invasion by malignant cells was evaluated through *ex vivo* bioluminescent imaging after immersing the harvested lungs in D-Luciferin solution (15 mg/mL) for 10 min. Concurrently, lung tissues were fixed in Bouin's fluid and subjected to H&E staining to assess pathological changes and evaluate the efficacy of the anti-metastatic treatment. Additionally, liver sections were also analyzed using H&E staining to provide a comprehensive assessment of metastasis. Tumor dimensions were documented, and H&E staining was performed to further analyze the tissue morphology.

In vivo antitumor evaluation

BALB/c mice were inoculated with 1×10^6 4T1 cells into the breast fat pad. Upon tumor volumes reaching approximately 100 mm^3, mice were divided into six groups and treated with Saline, NVs/T, V-NVs, V-NVs/A, V-NVs/T, V-NVs/T+A. Treatments were administered every two days for five cycles, with each dose containing 100 μg of NVs. After the last treatment, blood was collected for liver and kidney function analysis, and the mice were sacrificed for organ and tumor tissue collection. Tissues were fixed in 4 % paraformaldehyde for subsequent H&E staining, TUNEL assay, Ki67 analysis, and $CD8^+$ T cell immunofluorescence staining. Additionally, tumor tissues were homogenized in ice-cold PBS, and the supernatant was collected after centrifugation at 13,000 rpm for 15 min. The levels of TNF-α, INF-γ and IL-6 were then measured using the corresponding ELISA kits.

In vivo immunity

After the final treatment, tumor tissues were excised and cut into small pieces (2–4 mm). The tissue fragments were placed in a dissociation buffer containing 1 mg/mL collagenase type IV, 0.1 mg/mL DNase I, and 0.1 mg/mL hyaluronidase in RPMI-1640 medium. The samples were incubated at 37°C with gentle shaking for 1 h to generate single-cell suspensions. Following digestion, the tissues were mechanically dissociated using the rubber end of a syringe and filtered through a 70 μm strainer to remove debris. The resulting cell suspensions were treated with red blood cell lysing buffer to eliminate erythrocytes. For viability assessment, cells were stained with the Fixable Viability Stain 700 following the manufacturer's instructions.

To analyze tumor-infiltrating $CD8^+$ T cells ($CD45^+CD3^+CD8^+$) and regulatory T cells (Tregs, $CD45^+CD3^+CD4^+Foxp3^+$), cells were stained with anti-CD45-APC/Cy7, anti-CD3-FITC, anti-CD4-APC, and anti-CD8-PerCP/Cy5.5 antibodies according to the manufacturer's protocols. Following surface staining, cells were treated with a permeabilization buffer to allow intracellular staining. Intracellular markers were labeled using anti-Foxp3-PE antibodies. For the detection of tumor-infiltrating TNF-α^+CD8^+ T cells ($CD45^+CD3^+CD8^+$TNF-$^+$) and IFN-γ^+CD8^+ T cells ($CD45^+CD3^+CD8^+$ IFN-$^+$), cells were first stained with anti-CD45-APC/Cy7, anti-CD3-FITC, and anti-CD8-PerCP/Cy5.5 antibodies for surface markers. Subsequently, permeabilization and intracellular staining were performed using anti-TNF-α-APC and anti-IFN-γ-PE antibodies. To investigate macrophage subtypes within the tumor microenvironment, M1-like tumor-associated macrophages ($CD45^+CD11b^+F4/80^+CD80^+$) and M2-like tumor-associated macrophages ($CD45^+CD11b^+F4/80^+CD206^+$) were analyzed. Cells were labeled with anti-CD45-APC/Cy7, anti-F4/80-PerCP/Cy5.5, and anti-CD80-PE antibodies for surface markers. Intracellular staining for M2 macrophages was performed using anti-CD206-APC antibodies following permeabilization. For the assessment of dendritic cell (DC) maturation ($CD45^+CD11c^+CD86^+CD80^+$), tumor-draining lymph nodes were harvested and processed similarly. The cells were stained with anti-CD45-APC/Cy7, anti-CD11c-FITC, anti-CD86-APC, and anti-CD80-PE antibodies according to the manufacturer's protocols. The populations of immune cells in tumors and lymph nodes were finally determined with a flow cytometer and analyzed using FlowJo software.

CRediT authorship contribution statement

Fengxiang Liu: Resources, Methodology. **Yutong Lu:** Software, Methodology. **Lili Du:** Visualization, Project administration. **Jin Sun:** Writing – review & editing, Project administration, Funding acquisition. **Xia Wang:** Project administration, Methodology, Funding acquisition, Data curation. **Kaiyuan Wang:** Writing – review & editing, Supervision, Resources, Project administration, Funding acquisition. **Xiaoyuan Fan:** Resources, Methodology. **Jian Zhao:** Software, Formal analysis. **Ziqi Lin:** Visualization, Investigation, Data curation. **Wenwen Shen:** Supervision, Investigation. **Hao Zhang:** Supervision, Software. **Zhonggui He:** Resources, Funding acquisition. **Shipeng Ning:** Software, Project administration, Funding acquisition. **Jiaxin Lin:** Methodology. **Fei Sun:** Writing – original draft, Software, Project administration, Formal analysis, Conceptualization.

Declaration of Competing Interest

The authors declare that they have no known competing financial interests or personal relationships that could have appeared to influence the work reported in this paper.

Acknowledgements

This research was supported by National Natural Science Foundation of China (No. 82273874, 82404561, and 82303797), Liaoning Revitalization Talents Program (No. XLYC22202019), the China National Postdoctoral Program for Innovative Talents (BX20240233), the Postdoctoral Fellowship Program (Grade B) of China Postdoctoral Science Foundation (GZB20240179), the China Postdoctoral Science Foundation (No. 2023MD744230), Doctoral Scientific Research Launching Fund Project of Liaoning province (No. 2024-BS-075), Prospective Basic research project of 2024 Scientific Research Project of Liaoning Department of Education (LJ212410163042). TEM tests were supported by Beijing Zhongkebaice Technology Service Co., Ltd. (www.zkbaice.cn)

Appendix A. Supporting information

Supplementary data associated with this article can be found in the online version at doi:10.1016/j.nantod.2024.102604.

Data availability

Data will be made available on request.

References

[1] S. Zhu, Y. Wu, B. Song, M. Yi, Y. Yan, Q. Mei, K. Wu, Recent advances in targeted strategies for triple-negative breast cancer, J. Hematol. Oncol. 16 (2023) 100.
[2] Y. Liu, Y. Hu, J. Xue, J. Li, J. Yi, J. Bu, Z. Zhang, P. Qiu, X. Gu, Advances in immunotherapy for triple-negative breast cancer, Mol. Cancer 22 (2023) 145.
[3] Z. Lin, Y. Wang, W. Li, F. Sun, Q. Lv, S. Zhang, X. Liu, F. Qin, C. Luo, A natural compound-empowered podophyllotoxin prodrug nanoassembly magnifies efficacy-toxicity benefits in cancer chemotherapy, Asian J. Pharm. Sci. (2024).
[4] H. Zhang, T. Liu, Y. Sun, S. Wang, W. Wang, Z. Kuang, M. Duan, T. Du, M. Liu, L. Wu, F. Sun, J. Sheng, Z. He, J. Sun, Carbon-spaced Tandem-Disulfide bond bridge design addresses limitations of homodimer prodrug nanoassemblies: enhancing both stability and activatability, J. Am. Chem. Soc. 146 (2024) 22675–22688.
[5] P. Ghidotti, I. Petraroia, O. Fortunato, F. Pontis, Immunomodulatory role of EV-derived non-coding RNA in lung cancer, Extracell. Vesicles Circ. Nucleic Acids 4 (2023) 44–56.
[6] S.F. Shaitelman, W.A. Woodward, Neoadjuvant radioimmunotherapy synergy in triple-negative breast cancer: is microenvironment-guided patient selection on the horizon? Cancer Cell 42 (2024) 10–12.
[7] C. Luri-Rey, A. Manzanal, B. Pinci, A. Teijeira, Dendritic cells, headhunters for anti-tumor CD8(+) T cells in triple-negative breast cancer, Med 4 (2023) 341–343.
[8] X.Q. Wang, E. Danenberg, C.S. Huang, D. Egle, M. Callari, B. Bermejo, M. Dugo, C. Zamagni, M. Thill, A. Anton, S. Zambelli, S. Russo, E.M. Ciruelos, R. Greil, B. Gyorffy, V. Semiglazov, M. Colleoni, C.M. Kelly, G. Mariani, L. Del Mastro, O. Biasi, R.S. Seitz, P. Valagussa, G. Viale, L. Gianni, G. Bianchini, H.R. Ali, Spatial predictors of immunotherapy response in triple-negative breast cancer, Nature 621 (2023) 868–876.
[9] S. Ning, M. Lyu, D. Zhu, J.W.Y. Lam, Q. Huang, T. Zhang, B.Z. Tang, Type-I AIE photosensitizer loaded biomimetic system boosting cuproptosis to inhibit breast cancer metastasis and rechallenge, ACS Nano 17 (2023) 10206–10217.
[10] S. Ning, M. Suo, Q. Huang, S. Gao, K. Qiao, M. Lyu, Q. Huang, T. Zhang, B.Z. Tang, Biomimetic fusion liposomes boosting antitumor immunity and promote memory T cell differentiation to inhibit postoperative recurrence of breast cancer, Nano Today 54 (2024).
[11] Y. Huang, Y. Chen, S. Zhou, L. Chen, J. Wang, Y. Pei, M. Xu, J. Feng, T. Jiang, K. Liang, S. Liu, Q. Song, G. Jiang, X. Gu, Q. Zhang, X. Gao, J. Chen, Dual-mechanism based CTLs infiltration enhancement initiated by Nano-sapper potentiates immunotherapy against immune-excluded tumors, Nat. Commun. 11 (2020) 622.
[12] T. Wu, Y. Fu, S. Guo, Y. Shi, Y. Zhang, Z. Fan, B. Yang, B. Ding, Y. Liao, Self-assembly multifunctional DNA tetrahedron for efficient elimination of antibiotic-resistant bacteria, Aggregate 5 (2023).
[13] S. Sheng, X. Yu, G. Xing, L. Jin, Y. Zhang, D. Zhu, X. Dong, L. Mei, F. Lv, An apoptotic body-based vehicle with navigation for photothermal-immunotherapy by precise delivery and tumor microenvironment regulation, Adv. Funct. Mater. 33 (2022).
[14] J. Jiang, X. Cui, Y. Huang, D. Yan, B. Wang, Z. Yang, M. Chen, J. Wang, Y. Zhang, G. Liu, C. Zhou, S. Cui, J. Ni, F. Yang, D. Cui, Advances and prospects in integrated nano-oncology, Nano Biomed. Eng. 16 (2024) 152–187.
[15] M. Kumar, U. Kumar, A.K. Singh, Therapeutic nanoparticles: recent developments and their targeted delivery applications, Nano Biomed. Eng. 14 (2022).
[16] K. Wang, Y. Li, X. Wang, Z. Zhang, L. Cao, X. Fan, B. Wan, F. Liu, X. Zhang, Z. He, Y. Zhou, D. Wang, J. Sun, X. Chen, Gas therapy potentiates aggregation-induced emission luminogen-based photoimmunotherapy of poorly immunogenic tumors through cGAS-STING pathway activation, Nat. Commun. 14 (2023) 2950.
[17] K. Wang, X. Zhang, H. Ye, X. Wang, Z. Fan, Q. Lu, S. Li, J. Zhao, S. Zheng, Z. He, Q. Ni, X. Chen, J. Sun, Biomimetic nanovaccine-mediated multivalent IL-15 self-transpresentation (MIST) for potent and safe cancer immunotherapy, Nat. Commun. 14 (2023) 6748.
[18] S. Horie, Y. Watanabe, M. Ono, S. Mori, T. Kodama, Evaluation of antitumor effects following tumor necrosis factor-alpha gene delivery using nanobubbles and ultrasound, Cancer Sci. 102 (2011) 2082–2089.
[19] D. Laha, R. Grant, P. Mishra, N. Nilubol, The role of tumor necrosis factor in manipulating the immunological response of tumor microenvironment, Front Immunol. 12 (2021) 656908.
[20] Z. Ma, Y. Wang, H. He, T. Liu, Q. Jiang, X. Hou, Advancing ophthalmic delivery of flurbiprofen via synergistic chiral resolution and ion-pairing strategies, Asian J. Pharm. Sci. 19 (2024) 100928.
[21] J.X. Fan, Z.H. Li, X.H. Liu, D.W. Zheng, Y. Chen, X.Z. Zhang, Bacteria-mediated tumor therapy utilizing photothermally-controlled TNF-alpha expression via oral administration, Nano Lett. 18 (2018) 2373–2380.
[22] M. Zhuang, X. Chen, D. Du, J. Shi, M. Deng, Q. Long, X. Yin, Y. Wang, L. Rao, SPION decorated exosome delivery of TNF-alpha to cancer cell membranes through magnetism, Nanoscale 12 (2020) 173–188.
[23] H. Chen, H. Song, Y. Luo, C. Li, Y. Wang, J. Liu, F. Luo, H. Fan, X. Li, T. Sun, C. Jiang, Transcytosis mediated deep tumor penetration for enhanced chemotherapy and immune activation of pancreatic cancer, Adv. Funct. Mater. 33 (2023).
[24] H.D. Herce, D. Schumacher, A.F.L. Schneider, A.K. Ludwig, F.A. Mann, M. Fillies, M.A. Kasper, S. Reinke, E. Krause, H. Leonhardt, M.C. Cardoso, C.P. R. Hackenberger, Cell-permeable nanobodies for targeted immunolabelling and antigen manipulation in living cells, Nat. Chem. 9 (2017) 762–771.
[25] M. Souri, M. Soltani, F. Moradi Kashkooli, M.Kiani Shahvandi, Engineered strategies to enhance tumor penetration of drug-loaded nanoparticles, J. Control Release 341 (2022) 227–246.
[26] A. Moller, R.J. Lobb, The evolving translational potential of small extracellular vesicles in cancer, Nat. Rev. Cancer 20 (2020) 697–709.
[27] D. Iannotta, A. A, A.W. Kijas, A.E. Rowan, J. Wolfram, Entry and exit of extracellular vesicles to and from the blood circulation, Nat. Nanotechnol. 19 (2024) 13–20.
[28] Y. He, K. Wang, Y. Lu, B. Sun, J. Sun, W. Liang, Monensin enhanced generation of extracellular vesicles as transfersomes for promoting tumor penetration of pyropheophorbide-a from fusogenic liposome, Nano Lett. 22 (2022) 1415–1424.
[29] X. Wang, S. Ning, W. Tao, K. Wang, J. Li, L. Huang, S. Dong, Z. Fan, J. Zheng, Y. Li, B. Yang, Z. He, J. Sun, X. Chen, H. Liu, Cytomembrane-targeted photodynamic priming triggers extracellular vesicle storm for deep penetration and complete destruction of bladder cancer, Nano Today 56 (2024).
[30] Y. Yang, Y. Hong, G.H. Nam, J.H. Chung, E. Koh, I.S. Kim, Virus-mimetic fusogenic exosomes for direct delivery of integral membrane proteins to target cell membranes, Adv. Mater. 29 (2017).
[31] M. Han, B. Pang, C. Zhou, X. Li, Q. Wang, J. Jiang, Y. Li, Liquid biopsy of extracellular vesicle biomarkers for prostate cancer personalized treatment decision, Extracell. Vesicles Circ. Nucleic Acids (2022).
[32] R. Kalluri, K.M. McAndrews, The role of extracellular vesicles in cancer, Cell 186 (2023) 1610–1626.
[33] G. Raposo, P.D. Stahl, Extracellular vesicles, genetic programmers, Nat. Cell Biol. 26 (2024) 22–23.
[34] C. Liu, D. He, H. Cen, H. Chen, L. Li, G. Nie, Z. Zhong, Q. He, X. Yang, S. Guo, L. Wang, Z. Fan, Nucleic acid functionalized extracellular vesicles as promising therapeutic systems for nanomedicine, Extracell. Vesicles Circ. Nucleic Acids (2022).
[35] C. Burdziak, D. Alonso-Curbelo, T. Walle, J. Reyes, F.M. Barriga, D. Haviv, Y. Xie, Z. Zhao, C.J. Zhao, H.A. Chen, O. Chaudhary, I. Masilionis, Z.N. Choo, V. Gao, W. Luan, A. Wuest, Y.J. Ho, Y. Wei, D.F. Quail, R. Koche, L. Mazutis, R. Chaligne, T. Nawy, S.W. Lowe, D. Pe'er, Epigenetic plasticity cooperates with cell-cell interactions to direct pancreatic tumorigenesis, Science 380 (2023) eadd5327.
[36] S. Chen, D. Iannotta, M.L. O'Mara, J.P. Goncalves, J. Wolfram, Extracellular vesicle lipids in cancer immunoevasion, Trends Cancer 9 (2023) 883–886.
[37] Z. Zhuo, J. Wang, Y. Luo, R. Zeng, C. Zhang, W. Zhou, K. Guo, H. Wu, W. Sha, H. Chen, Targeted extracellular vesicle delivery systems employing superparamagnetic iron oxide nanoparticles, Acta Biomater. 134 (2021) 13–31.
[38] Q. Zhou, C. Dong, W. Fan, H. Jiang, J. Xiang, N. Qiu, Y. Piao, T. Xie, Y. Luo, Z. Li, F. Liu, Y. Shen, Tumor extravasation and infiltration as barriers of nanomedicine for high efficacy: The current status and transcytosis strategy, Biomaterials 240 (2020) 119902.
[39] X. Chen, M. Zhao, Q. Xie, S. Zhou, X. Zhong, J. Zheng, R. Yang, X. Du, J. Xia, Y. Liao, Click-hydrogel delivered aggregation-induced emissive nanovesicles for simultaneous remodeling and antibiosis of deep burn wounds, Aggregate 5 (2023).
[40] C. Liu, X. Liu, X. Xiang, X. Pang, S. Chen, Y. Zhang, E. Ren, L. Zhang, X. Liu, P. Lv, X. Wang, W. Luo, N. Xia, X. Chen, G. Liu, A nanovaccine for antigen self-presentation and immunosuppression reversal as a personalized cancer immunotherapy strategy, Nat. Nanotechnol. 17 (2022) 531–540.
[41] L. Wang, G. Wang, W. Mao, Y. Chen, M.M. Rahman, C. Zhu, P.M. Prisinzano, B. Kong, J. Wang, L.P. Lee, Y. Wan, Bioinspired engineering of fusogen and targeting moiety equipped nanovesicles, Nat. Commun. 14 (2023) 3366.
[42] H. Yan, H. Shen, J. SiTu, Y. Yang, L. Zhang, K. Yang, Preparation of Bmi-1-siRNA lipid nanoparticles and effects in gastric cancer, Nano Biomed. Eng. (2024).
[43] L.L. Huang, W. Wang, Z. Wang, H. Zhang, H. Liu, G. Wu, W. Nie, H.Y. Xie, Engineering oncolytic adenoviruses with VSVG-decorated tumor cell membranes for synergistically enhanced antitumor therapy, Adv. Funct. Mater. 33 (2022).
[44] Y. Fu, S. Xiong, Tagged extracellular vesicles with the RBD of the viral spike protein for delivery of antiviral agents against SARS-COV-2 infection, J. Control Release 335 (2021) 584–595.
[45] J. Zhang, A. Brown, B. Johnson, D. Diebold, K. Asano, G. Marriott, B. Lu, Genetically engineered extracellular vesicles harboring transmembrane scaffolds exhibit differences in their size, expression levels of specific surface markers and cell-uptake, Pharmaceutics 14 (2022).
[46] R. Tenchov, J.M. Sasso, X. Wang, W.S. Liaw, C.A. Chen, Q.A. Zhou, Exosomes horizontal line Nature's lipid nanoparticles, a rising star in drug delivery and diagnostics, ACS Nano 16 (2022) 17802–17846.
[47] H. Tan, K. Mao, X. Cong, Y. Xin, F. Liu, J. Wang, X. Wang, J. Han, Y. Zhang, Y. G. Yang, T. Sun, In vivo immune adjuvant effects of CaCO(3) nanoparticles through intracellular Ca(2+) concentration regulation, ACS Appl. Mater. Interfaces 15 (2023) 39157–39166.
[48] L. Guo, J. Ding, W. Zhou, Converting bacteria into autologous tumor vaccine via surface biomineralization of calcium carbonate for enhanced immunotherapy, Acta Pharm. Sin. B 13 (2023) 5074–5090.
[49] J. An, M. Liu, L. Zhao, W. Lu, S. Wu, K. Zhang, J. Liu, Z. Zhang, J. Shi, Boosting tumor immunotherapy by bioactive nanoparticles via Ca2+ interference mediated TME reprogramming and specific PD-L1 depletion, Adv. Funct. Mater. 32 (2022).
[50] Y. Li, S. Gong, W. Pan, Y. Chen, B. Liu, N. Li, B. Tang, A tumor acidity activatable and Ca(2+)-assisted immuno-nanoagent enhances breast cancer therapy and suppresses cancer recurrence, Chem. Sci. 11 (2020) 7429–7437.

[51] C.Y. Soo, Y. Song, Y. Zheng, E.C. Campbell, A.C. Riches, F. Gunn-Moore, S.J. Powis, Nanoparticle tracking analysis monitors microvesicle and exosome secretion from immune cells, Immunology 136 (2012) 192–197.
[52] J. Bai, J. Duan, R. Liu, Y. Du, Q. Luo, Y. Cui, Z. Su, J. Xu, Y. Xie, W. Lu, Engineered targeting tLyp-1 exosomes as gene therapy vectors for efficient delivery of siRNA into lung cancer cells, Asian J. Pharm. Sci. 15 (2020) 461–471.
[53] L. Alvarez-Erviti, Y. Seow, H. Yin, C. Betts, S. Lakhal, M.J. Wood, Delivery of siRNA to the mouse brain by systemic injection of targeted exosomes, Nat. Biotechnol. 29 (2011) 341–345.